Nanoscale Advances

ROYAL SOCIETY OF CHEMISTRY

PAPER

View Article Online
View Journal | View Issue

Cite this: *Nanoscale Adv.*, 2022, **4**, 2704

$MnMoO_4$-S nanosheets with rich oxygen vacancies for high-performance supercapacitors†

Hao Fu, Meixin Wang, Qing Ma, Mingwen Wang, Xiping Ma and Yaping Ye *

The structure of materials is closely related to their electrochemical properties. $MnMoO_4$ materials have good stability as supercapacitors but their specific capacitance performance is not excellent. To improve electrochemical performance of $MnMoO_4$, this study conducts secondary hydrothermal treatment in thiourea solution on $MnMoO_4$ electrode material grown on nickel foam synthesized by traditional hydrothermal method. A more compact S-doped $MnMoO_4$ electrode material with more oxygen vacancies and higher specific capacitance was obtained. At the current density of 1 A g^{-1}, the specific capacitance of the composite material reached 2526.7 F g^{-1}, which increased by 140.9% compared with that of ordinary $MnMoO_4$ material. The capacitance retention rate of the composite material was 95.56% after 2000 cycles at 10 A g^{-1}. An asymmetric supercapacitor was fabricated using S-doped $MnMoO_4$ as the positive electrode, activated carbon as the negative electrode, and 6 mol L^{-1} KOH solution as the electrolyte. The specific capacitance of the assembled supercapacitor was 117.50 F g^{-1} at 1 A g^{-1}, and a high energy density of 47.16 W h kg^{-1} at the power density of 849.98 W kg^{-1} was recorded. This method greatly improves the specific capacitance of $MnMoO_4$ through simple processing, which makes it have great application potential.

Received 6th March 2022
Accepted 24th April 2022

DOI: 10.1039/d2na00148a

rsc.li/nanoscale-advances

Introduction

The supercapacitor is a kind of energy storage device whose capacity, power density, and energy density are between lithium battery and traditional capacitor.[1–3] With the increasing consumption of traditional energy resources, environmental problems attract considerable attention in modern society, making green-energy-related technologies hot topics in both scientific and industrial fields. Among them, the storage of electricity is in the first tier because our current life is more or less dependent on electronic devices.[4,5] With higher efficiency than the traditional capacitor, supercapacitors have been demonstrated as promising energy storage devices because of their small size, large capacity, and high energy density. A supercapacitor is typically composed of electrolyte, separator, and positive/negative electrodes connected with a fluid collector.[6,7] The key to a practical application of supercapacitors is to find/synthesize an effective electrode. Thus, there is always a quest to fabricate or find a solid electrode with high specific capacitance as well as stability. As the most critical part of a supercapacitor, electrodes can be built with a wide variety of materials, including carbons, metal oxides, and polymers, and these different types of electrode materials bring in completely different performances of devices.[8] Transition metal oxides, such as MnO_2, NiO, Co_3O_4, MoO_3, *etc.*,[9–12] have been studied extensively as electrode materials, whose specific capacitance and cycling stability are superior to carbon materials and organic polymers, respectively.[13,14] For single metal oxide material, the highest specific capacitance was recorded in RuO_2. Later, binary transition metal oxides, such as $MMoO_4$, $MCoO_2$, MFe_2O_4, *etc.*[15–17] (where M is another transition metal), were explored as electrode materials and presented improving properties, including better electronic conductivity, higher specific capacitance, lower intercationic charge transfer activation energy, higher structural stability, and more active sites for rapid reversible Faraday reaction.[18,19] Thus, more and more efforts were donated to this catalog of materials for novel supercapacitor electrodes. The specific capacitance of the transition metal depends on the oxidation states of the transition metals, the quantity of non-stoichiometric oxygen, and the presence of defect structure. The oxygen vacancies are favorable for electron migration because they can enhance the mobility of lattice oxygen. The textural properties and phase purity of transition metals depend upon the preparation methods. Recently, $MnMoO_4$ has attracted extraordinary attention because of its good structural stability and circularity.[20] For example, Mu *et al.* synthesized $MnMoO_4$ nanosheets on nickel foam *via* a one-step hydrothermal route, obtaining a specific capacitance of 1271 F g^{-1} at a scanning rate of 5 mV s^{-1} with a cycle retention rate of 84.5% of the initial specific capacitance after 2000 cycles.[21] Cao *et al.* synthesized nanocrystalline rod-

Beijing Key Laboratory for Science and Application of Functional Molecular and Crystalline Materials, University of Science and Technology Beijing, Beijing 100083, China. E-mail: yypfree@sas.ustb.edu.cn

† Electronic supplementary information (ESI) available. See https://doi.org/10.1039/d2na00148a

like $MnMoO_4$ by co-precipitation method. The specific capacitance at a current density of 1 A g^{-1} was 109 C g^{-1}, which maintained 86% of the initial capacity after 2000 charge–discharge cycles.[22]

Some recent studies demonstrated that the introduction of S, P, and other anions into binary transition metal oxides can enhance the electrical conductivity, increase the number of oxygen vacancies, and improve the ability of the material to store electrons.[23,24] Replacement of O by S allows for more unique tiny structures and more abundant redox reactions, which can reduce the expansion and contraction pressures in nanostructures during continuous charge–discharge processes, resulting in an enhanced cycle life.[24] For example, Xie *et al.* prepared a core–shell structure of Ni_3S_2 wrapped by $MnMoO_4$ *via* a secondary hydrothermal method followed by annealing treatment. At a current density of 1 mA cm^{-2}, a specific capacity of 979.3 C g^{-1} was recorded and 88.3% of the capacity was retained after 7000 charge–discharge cycles at 10 mA cm^{-2}.[25] Shiva Alipour *et al.* used the secondary hydrothermal method to replace all the O in $MnMoO_4$ with Na_2S to generate $MnMoS_4$ as the electrode material for a supercapacitor, giving a specific capacitance up to 1865.2 F g^{-1}.[26] Xiang *et al.* synthesized $CoMoO_4$ nanomaterials by the hydrothermal method, then the material was doped with P by vapor deposition, in which O in the lattice was replaced by P, leaving vacancies accordingly. The obtained P-$CoMoO_4$ material showed excellent electrochemical properties with a specific capacitance of 1368 C g^{-1} at a current density of 2 A g^{-1}. After 5000 cycles of charge and discharge, 95.3% of initial capacity was maintained.[27] So far, there are no attempts to use a few S to replace O in $MnMoO_4$ to increase the number of oxygen vacancies, so as to improve the specific capacitance of the material on the doping and substitution of anions in $MnMoO_4$ materials.

In this study, $MnMoO_4$ nanosheets were first grown *in situ* on nickel foam through the hydrothermal method. Then, the prepared $MnMoO_4$ was treated by a secondary hydrothermal method in thiourea solution at a lower temperature so that a small amount of O was displaced by S, and the S-doped $MnMoO_4$-S nanosheets with more oxygen vacancies were synthesized. It was proved that S successfully replaced a few parts of O and produced more oxygen vacancies in the secondary hydrothermal S-transformation process. The electrochemical testing results showed that the specific capacitance of $MnMoO_4$-S at 1 A g^{-1} was as high as 2526.7 F g^{-1}, which was 2.4 times that of $MnMoO_4$ (1050.0 F g^{-1}). Moreover, 95.56% of the initial capacity can be maintained after 2000 charge–discharge cycles at 10 A g^{-1}, which makes S-doped MnMoO4-S a promising electrode material for supercapacitors.

Experiments

Synthesis of $MnMoO_4$ precursors and $MnMoO_4$-S

The Ni foam was cut into pieces of 2 cm × 1.5 cm, and the possible oxides on the surface were removed by ultrasound in 3 M hydrochloric acid for 15 min. Then, the pretreated Ni foam was washed with deionized water and ethanol 3 times and vacuum-dried at 60 °C for 12 h. Two aqueous solutions of $Na_2MoO_4 \cdot 2H_2O$ and $MnCl_2$ in deionized water were prepared by dissolving 1.5 mmol of the salts in 15 mL water. The two solutions were freshly mixed, stirred for 1 h, and then transferred to the inner tank of a 50 mL PTFE reactor. The purpose of this step was to reduce the size of crystal particles. To get a homogeneous film on the Ni foam, a custom-made PTFE rack (Fig. S1†) was settled into the reactor to hold the Ni foam. The reactor was heated in an electric blast drying oven at 150 °C for 8 h and $MnMoO_4$ precursors were obtained. Precursors were taken out after the reaction was completed and cooled to room temperature, washed with ultrasonic deionized water several times, and dried in a vacuum drying oven at 60 °C. The $MnMoO_4$ precursors prepared in the previous step were added into a 50 mL PTFE reactor with 30 mL 0.05 M thiourea solution, heated at 90 °C for 6 h, and taken out after cooling. Then, they were washed with ultrasonic deionized water several times and dried in a vacuum oven at 60 °C. The products were labeled as $MnMoO_4$-S after secondary hydrothermal synthesis.

The reaction for hydrothermal synthesis of $MnMoO_4$ is shown in eqn (1), and the chemical equation for the possible vulcanization process is shown in eqn (2) and eqn (3).

$$Mn^{2+} + MoO_4^{2-} \rightarrow MnMoO_4 \quad (1)$$

$$CS(NH_2)_2 + H_2O \rightarrow CO(NH_2)_2 + H_2S \quad (2)$$

$$MnMoO_4 + xH_2S \rightarrow MnMoO_{4-x}S_x + xH_2O \quad (3)$$

$MnMoO_4$-S//AC asymmetric supercapacitor assembly

The required amount of activated carbon (AC) was calculated according to eqn (4).[28] The AC, conductive carbon black, and polyvinylidene fluoride (PVDF) with a mass ratio of 8 : 1 : 1 were added to 1 mL *N*-methylpyrrolidone, which was stirred into a paste at room temperature. The paste was evenly smeared on the Ni foam treated with hydrochloric acid. The activated carbon anode material was obtained by vacuum drying at 60 °C for 12 h. Using the prepared $MnMoO_4$-S as the positive electrode, AC as the negative electrode, and 6 M KOH as electrolyte, an asymmetric supercapacitor simulation assembly was carried out in a beaker.

$$\frac{m^+}{m^-} = \frac{C^- \times \Delta V^-}{C^+ \times \Delta V^+} \quad (4)$$

where m^+ and m^- are the effective mass of AC and $MnMoO_4$-S, ΔV^+ and ΔV^- are the potential window of $MnMoO_4$-S and AC in cyclic voltammetry scanning, respectively. C^+ and C^- are, respectively, the capacitance of $MnMoO_4$-S and AC (F g^{-1}) calculated according to the cyclic voltammetry curve, and the calculation formula is shown in eqn (5).[29]

$$C_s = \frac{\int I(V)\mathrm{d}V}{m \times \Delta V \times S} \quad (5)$$

C_s is the capacitance, the integral part is the area of the cyclic voltammetry curve, m is the mass of the active material, ΔV is the potential window of cyclic voltammetry scanning, and S is the scanning rate (V s^{-1}).

Characterization of materials

Scanning electron microscopy (SEM), transmission electron microscopy (TEM), X-ray diffraction (XRD), energy dispersive spectrometer (EDS), laser Raman co-focal microspectrometry (Raman), and X-ray photoelectron spectroscopy (XPS) were used to characterize the secondary hydrothermal products. The electrochemical characterization was performed by cyclic voltammetry (CV), galvanostatic charge–discharge (GCD), and electrochemical impedance spectroscopy (EIS). The microtopography of prepared materials was observed by SEM (JSM-7800Fprime, JEOL), corresponding element distribution was observed by EDS (Aztec X-MaxN50, Oxford), and crystal structure was observed by TEM. The crystal structure was also characterized by XRD (Ultimaiv, Rigaku), and the valence states of elements were analyzed by XPS (Axis Ultradld, Kratos). The composition was further determined by Raman spectroscopy (Horiba Labram HR, Horiba). Electrochemical tests such as CV, GCD, and EIS were carried out using an electrochemical workstation (PARSTAT4000A, AMETEK).

Results and discussion

Structural characterization

In order to dig out differences in the products after primary hydrothermal and secondary hydrothermal treatments, SEM was used to observe the morphology of the materials. First of all, to demonstrate the growth of our material, Ni foam pretreated with hydrochloric acid was observed (Fig. S2†). It can be seen that the surface of the nickel foam is pretty smooth. According to Fig. 1a–c, the morphology of $MnMoO_4$ precursor on Ni foam at different resolutions was presented. It can be seen that the hydrothermal $MnMoO_4$ materials are in the shape of nanosheets, which uniformly and compactly cover the surface of nickel foam. This structure can reduce the dead volume of electrode materials and increase the electron conduction efficiency in electrochemical behavior.[30] Moreover, a small number of nanosheets cluster together to emerge in a flower shape. The morphology of $MnMoO_4$-S on Ni foam after secondary hydrothermal treatment in thiourea solution is shown in Fig. 1d–f. The morphology does not change greatly, but the nanosheets become denser, and the distance between sheets becomes smaller. In addition to the flowers formed by the agglomeration of nanosheets, some nanocones with smaller sizes also can be observed, as shown in Fig. 1g–i. These changes lead to a larger surface area of the electrode materials after the secondary hydrothermal treatment and a much fuller contact with the electrolyte, which is conducive to improving the electrochemical activity.[31,32]

EDS was used to analyze the composition and proportion of elements in materials with different morphologies of synthetic products. Fig. 2a shows an overall EDS diagram of $MnMoO_4$ at low magnification. It can be seen that Mn, Mo, O, and S are uniformly distributed on the surface of the nickel foam. Fig. 2b is the EDS diagram of flower-like nanosheets selected to be enlarged, showing that Mn, Mo, O, and S are also uniformly distributed in this flower structure. Fig. 2c is the surface scanning EDS diagram of a nanocone structure at a large magnification. It can be seen that the ratio of S element and Mo element in this area increase significantly, while the ratio of Mn and O elements has subtle changes. Table S1† shows the elemental content analysis from the EDS test. The atomic concentration ratio of Mo : Mn is close to 1 : 1, and Mn : O is close to 1 : 3.7, which is consistent with the elemental distribution of $MnMoO_4$, theoretically. The content of S is little but evenly distributed in the material, which proves that the $MnMoO_4$-S crystal is mainly composed of $MnMoO_4$ with a few S atoms replaced by O in the lattice. The distribution of elements in the flower structure is similar to that of the whole matrix. The content of S in nanocones increases while the content of O decreases. It can be explained that more S displaces O in these regions, leading to the change of crystal structure as well.

To further understand the structure, TEM was used to observe fine crystal structures. Fig. 3a and b are the transmission electron microscopy images of $MnMoO_4$. Fig. 3a shows that $MnMoO_4$ is flake-like, and the lattice spacing of 0.28 nm can be seen after amplification in Fig. 3b, which corresponds to the (111) crystal plane of $MnMoO_4$.[33] Fig. 3c is the selected area

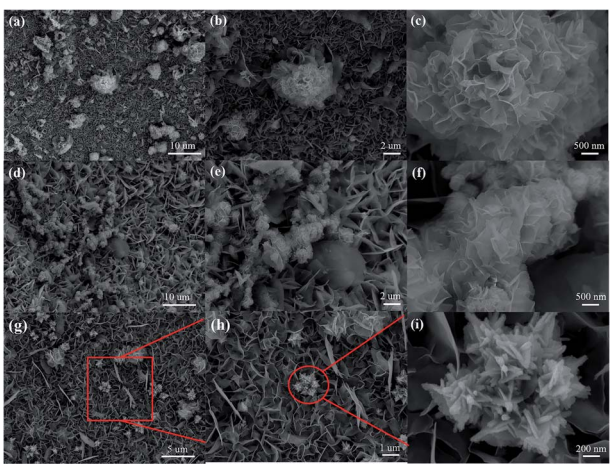

Fig. 1 Low and high magnified SEM images of (a–c) $MnMoO_4$ nanosheets, (d–f) $MnMoO_4$-S nanosheets, and (g–i) $MnMoO_4$-S nanocones.

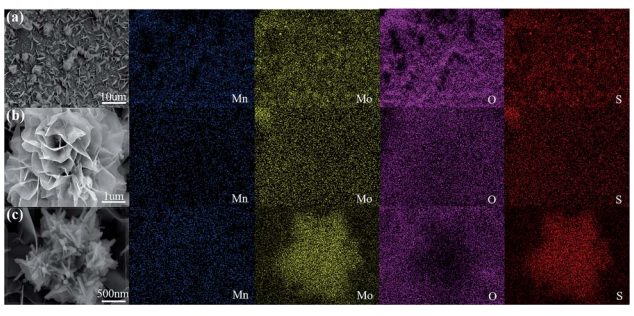

Fig. 2 EDS elemental mapping images of a selected area of $MnMoO_4$-S, (a) the overall surface, (b) flower composed of nanosheets, (c) nanocone.

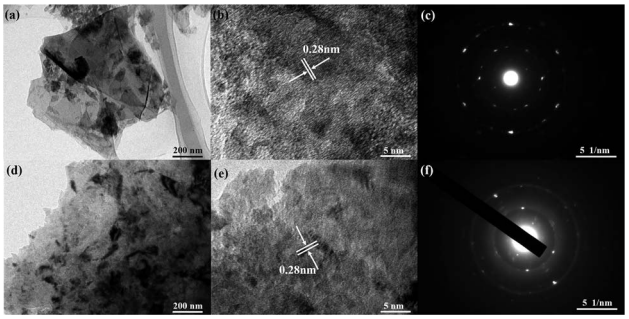

Fig. 3 Low and high magnified TEM images of (a and b) $MnMoO_4$, (d and e) $MnMoO_4$-S, the SAED of (c) $MnMoO_4$-S, (f) $MnMoO_4$-S.

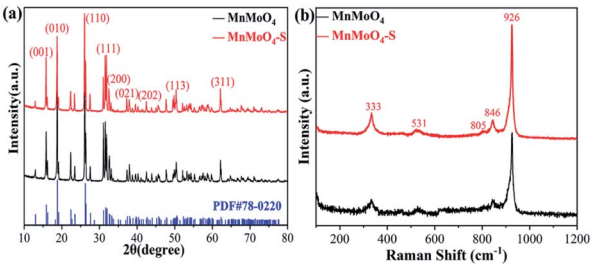

Fig. 5 (a) The XRD patterns of the $MnMoO_4$ and $MnMoO_4$-S (b) The Raman shift patterns of the $MnMoO_4$ and $MnMoO_4$-S.

electron diffraction (SAED) pattern of $MnMoO_4$, and its light spots are scattered, which proves the single-crystal nature of the material.[22] Fig. 3d–e are TEM results of $MnMoO_4$-S. It can be seen that $MnMoO_4$-S is also flake-like as shown in Fig. 3d. In addition, lattice fringe spacing of 0.28 nm is also observed in Fig. 3e. Fig. 3f is the SAED result of $MnMoO_4$-S. Different from the result of $MnMoO_4$, its light spots are circular, which demonstrates the polycrystalline nature of the material.[34] These results are consistent with those of SEM and EDS.

In order to know the surface properties of synthetic materials, we conducted the BET test, and the results are shown in Fig. 4. Both $MnMoO_4$ and $MnMoO_4$-S have the properties of mesoporous materials. The specific surface area of the material increased from 1.2100 $m^2\ g^{-1}$ to 1.4182 $m^2\ g^{-1}$ after secondary hydrothermal treatment. In addition, the average pore size decreased from 15.0469 nm to 14.2910 nm, which was consistent with the conclusion that nanosheets became dense as observed in SEM. The cumulative pore volume of the material increased from 0.004552 $cm^3\ g^{-1}$ to 0.005067 $cm^3\ g^{-1}$ after secondary hydrothermal treatment. $MnMoO_4$-S with a larger specific surface area and more nanosheets could provide abundant active sites for faradaic reactions, so it is favourable for energy storage.[35]

Because the diffraction of Ni foam itself is too strong, the solid powder at the bottom of the hydrothermal reactor was selected for XRD tests. The results are shown in Fig. 5a. $MnMoO_4$ crystal was successfully synthesized through the hydrothermal method, which completely corresponds to the absorption peak of $MnMoO_4$ in standard card PDF# 78-0220.[33] The strong diffraction peaks appear when 2θ is 13.023°, 15.891°, 26.217°, 31.994°, 32.779°, 53.496°,and 62.575°,respectively, corresponding to the crystal faces of (0,0,1), (0,1,0), (1,1,0), (1,1,1), (2,0,0), (1,1,3), and (3,1,1), which belong to $MnMoO_4$, demonstrating the successful synthesis of $MnMoO_4$. The diffraction pattern does not change briefly after the secondary hydrothermal process, indicating that the main composition of our synthetic material is $MnMoO_4$, and it also indicates that only a small amount of S is doped in the secondary hydrothermal process. Therefore, the composition of the synthesized material is uniform rather than composite material, and this is beneficial to its electrochemical cycling stability. In order to confirm that S is indeed doped into the crystal structure, we read the strongest peak data of typical diffraction peaks in the two groups of original test data for comparison (Tabel S2†). It can be found that each diffraction peak angle of the material after the secondary hydrothermal process is slightly offset to the direction of 2θ decreased. The offset range is very small and less than 0.1°, so no obvious difference can be seen from the pattern. But it is obvious that these delicate differences are caused by the S doping. The crystal cell parameters of the two materials were analyzed by MDI JADE software (Tabel S3†). It can be found that both the crystal cell length and volume of $MnMoO_4$-S changed slightly, the lengths changed from 5.775 Å, 5.977 Å, and 6.937 Å to 5.801 Å, 5.969 Å, and 5.947 Å, and the crystal cell volume increased from 222.18 $Å^3$ to 223.71 $Å^3$. This is because the S element with a larger radius replaces the original position of O, which leads to cell expansion and changes in cell parameters. In addition, the crystallinity of the material decreases slightly from 99.13% to 99.11%, which is consistent with the results observed by TEM. The Ni foam with $MnMoO_4$-S growth was observed in a high-speed high-resolution confocal microscopy Raman spectrometer (Horiba HR, France), and its Raman image is shown in Fig. 5b, which was similar to the previous literature on $MnMoO_4$.[36] The peaks at 333 cm^{-1}, 531 cm^{-1} were attributed to the bending vibration of the Mo–O bond, and the peaks at 846 cm^{-1}, 926 cm^{-1} were attributed to the stretching vibration of the Mo–O bond. Raman image did not show the vibration absorption peak of the Ni–S bond, which proved that thiourea did not react with nickel foam to generate NiS_x in the secondary hydrothermal process at low temperature, further supporting the fact that only a small part of S displaced the position of O after the secondary hydrothermal process. The vibration of the Mo–S bond cannot be detected due to only a small amount of S incorporation.

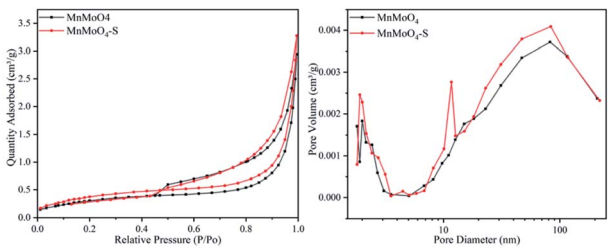

Fig. 4 BET and BJH curves of MnMoO4 and MnMoO4-S.

In order to further determine the valence states of each element, XPS measurement was performed on the electrode

materials, as shown in Fig. 6a. The binding energy peaks of 643.22 eV and 651.83 eV in Fig. 6b correspond to the $2p_{1/2}$ and $2p_{3/2}$ electron orbits of Mn^{2+}, respectively, which proves that Mn element exists in the form of Mn^{2+}.[37,38] The binding energy peaks of 234.64 eV and 231.62 eV in Fig. 6c correspond to the $3d_{3/2}$ and $3d_{5/2}$ electron orbits of Mo^{6+}, respectively, which demonstrate that Mo mainly exists in the form of Mo^{6+};[39,40] the peaks at the lower binding energies of 234.30 eV and 231.14 eV correspond to the $3d_{3/2}$ and $3d_{5/2}$ electron orbitals of Mo^{5+}, respectively, indicating the existence of Mo^{5+};[41] The peaks at the lower binding energies of 232.68 eV and 230.59 eV correspond to the $3d_{3/2}$ and $3d_{5/2}$ orbitals of Mo^{4+}, respectively, and the obvious peaks at the lower binding energies of 225.06 eV correspond to the 2s orbital of S^{2-}.[42–44] In Fig. 6d, the absorption peaks of binding energies 532.17 eV, 530.79 eV, and 529.81 eV correspond to surface hydroxyl group, oxygen vacancy, and lattice oxygen, respectively.[45] The proportion of peak area of oxygen vacancy in synthesized $MnMoO_4$-S is larger than that of undoped $MnMoO_4$ (Fig. S3†), indicating that more oxygen vacancies are formed during the secondary hydrothermal process. The possible reasons for the generation of oxygen vacancy are as follows: (1) compared with O^{2-}, S^{2-} has a larger volume and transfer and diffusion resistance and a smaller transfer rate, so that O falls off from the crystal lattice and S does not have enough time to enter the crystal lattice when exchange occurs; (2) Mo^{6+} combined with S is unstable and tends to become the more stable Mo^{4+}, which makes a part of Mo tend to keep a low valence after the incorporation of S, resulting in the escape of some oxygen atoms and the formation of oxygen vacancies; (3) a high oxygen binding energy indicates a weak Coulomb force between the metal cation and the oxygen anion, which may contribute to the formation of oxygen vacancies and the improvement of oxygen mobility.[46,47] In Fig. 6e, the binding energies of 161.11 eV and 164.19 eV correspond to the $2p_{1/2}$ and $2p_{3/2}$ orbitals of S^{2-}, indicating that S exists in the form of S^{2-}.

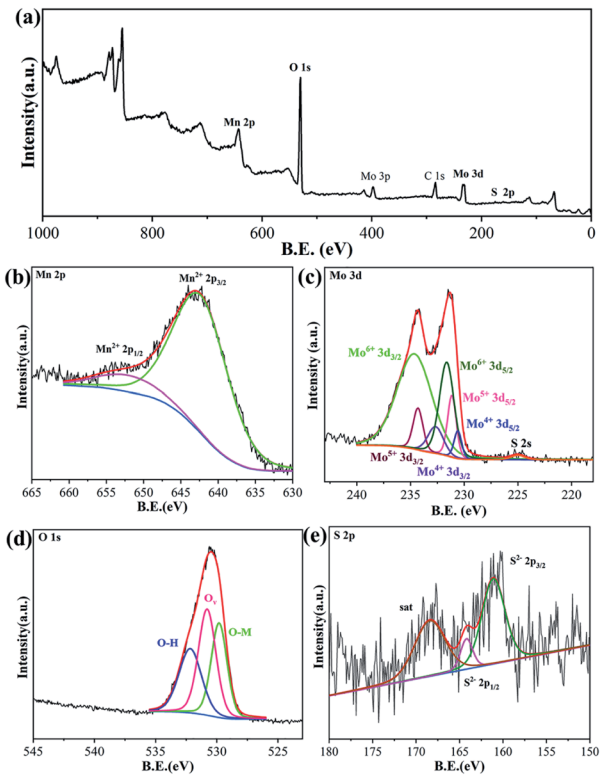

Fig. 6 XPS spectra of $MnMoO_4$-S (a) full-scan survey, (b) Mn 2p, (c) Mo 3d, (d) O 1s, (e) S 2p.

Electrochemical property characterization

To explore the electrochemical properties of the synthetic materials, conventional three-electrode system tests were carried out firstly. The Ni foams with $MnMoO_4$ and $MnMoO_4$-S materials clamped by platinum sheet electrode were used respectively as the working electrode, platinum wire electrode as the counter electrode, calomel electrode as the reference electrode, and 30 mL 1 M KOH solution as the electrolyte. The tests were performed with PARSTAT4000A electrochemical workstation.

Fig. 7a shows the CV curves of $MnMoO_4$ and $MnMoO_4$-S between the potential window of 0.1–0.5 V, among which the active materials loaded on the two electrodes were 0.8 mg and 1 mg, respectively. It can be seen that there are obvious symmetrical oxidation peaks and reduction peaks in CV curves, indicating that reversible redox reactions have occurred in both materials on the electrode. The reversible redox reaction is the main reason for the generation of pseudocapacitance, which therefore means that both $MnMoO_4$ and $MnMoO_4$-S have obvious pseudocapacitance. The CV plot area of $MnMoO_4$-S is larger than that of $MnMoO_4$, indicating that $MnMoO_4$-S has more possibilities of redox reaction and greater pseudocapacity. Fig. 7b is the CV diagram of $MnMoO_4$-S at different scanning speeds. With the increase in scanning speed, the oxidation peak of the CV curve moves to the positive direction, and the reduction peak moves to the negative direction, which is caused by polarization. The CV curves at different scanning velocities are similar, which indicates that the redox reaction of the material has good reversibility so that rapid and reversible electron transfer can occur at the interface between the electrode material and electrolyte. Therefore, the electrode material can be charged and discharged rapidly. The reason for the generation of the pseudocapacitance of $MnMoO_4$ can be expressed by eqn (6) and (7). According to the previous literature, Mo^{6+} does not participate in the redox reaction.[48] However, the valence of Mo changes after S-doped, which increases the possibility of the reactions of eqn (8) and (9). The valence changes of Mo elements contribute to the pseudocapacitance of the material, which is an important reason for the increase of its capacitance.

$$MnO + OH^- \rightarrow MnOOH + e^- \quad (6)$$

$$MnOOH + OH^- \rightarrow MnO(OH)_2 + e^- \quad (7)$$

$$Mo^{6+} + e^- \rightarrow Mo^{5+} \quad (8)$$

$$Mo^{5+} + e^- \rightarrow Mo^{4+} \quad (9)$$

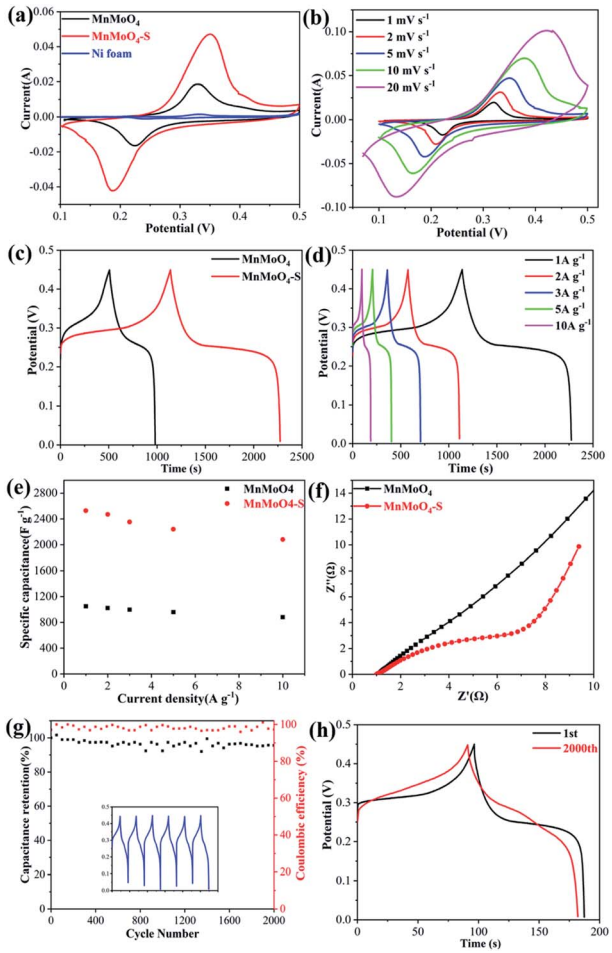

Fig. 7 (a) CV curves of $MnMoO_4$, $MnMoO_4$-S, and Ni foam at the scan rate of 5 mV s^{-1}; (b) CV curves of the $MnMoO_4$-S at various scan rates; (c) GCD curves of $MnMoO_4$-S and $MnMoO_4$ under the current densities of 1 A g^{-1}; (d) GCD curves of $MnMoO_4$-S under different current densities; (e) specific capacitance at different current densities; (f) Nyquist plots of $MnMoO_4$-S and $MnMoO_4$; (g) cycling stability of the $MnMoO_4$-S at 10 A g^{-1} and the inset shows GCD patterns of last 6 cycles; (h) the first and the last cycle of 2000 cycles.

Fig. 7c is the charge–discharge diagram of $MnMoO_4$-S at a constant current density of 1 A g^{-1}. Under the same current density, compared with $MnMoO_4$, $MnMoO_4$-S has a larger charging and discharging platform and a longer charging and discharging time, resulting in a larger specific capacitance of material. According to eqn (10), the specific capacitance of the $MnMoO_4$-S at 1 A g^{-1} is 2526.7 F g^{-1}, while the specific capacitance of $MnMoO_4$ is 1048.8 F g^{-1} at 1 A g^{-1}, which is increased by 140.9% after S doping. Fig. 7d shows the charge–discharge curves of electrode materials at different current densities. It can be seen that the charging and discharging platforms corresponding to the occurrence of redox reactions always exist, which also proves the existence of pseudocapacitance and further proves the reversibility of redox reactions occurring in materials. According to the GCD curve of current density 1 A g^{-1}, 2 A g^{-1}, 3 A g^{-1}, 5 A g^{-1}, and 10 A g^{-1}, the corresponding specific capacitance was calculated as 2526.7 F g^{-1}, 2468.9 F g^{-1}, 2351.7 F g^{-1}, 2241.2 F g^{-1}, and 2081.2 F g^{-1}. The calculated specific capacitance decreases to 82.37% as the current density increases from 1 A g^{-1} to 10 A g^{-1}. This is because the reaction rate is too fast, and the redox reaction and intercalation reaction occur incompletely at a larger current density.[49]

$$C_s = \frac{\int I dt}{m \Delta V} \quad (10)$$

The electrode was charged and discharged for 2000 cycles at 10 A g^{-1}. The results are shown in Fig. 7f. After 2000 cycles, the specific capacitance retention rate of the material was 95.56%, which proved that the electrode material had good stability. Fig. 7g shows the charge–discharge curves of the 2000th and 1st cycle with a slight deformation, which is caused by the slight deformation of the nanostructure of the electrode material and the change of the concentration of the electrolyte during the long cycle. However, the charge–discharge platform representing oxidation and reduction reactions still exists, indicating that the pseudocapacitance is not greatly affected. Fig. 7h is the Nyquist diagram of $MnMoO_4$ and $MnMoO_4$-S. Both materials grow on the Ni foam, so the contact resistance is very small, which is reflected in the intersection of the impedance curve and the horizontal axis. The diameter of the semicircle in the high-frequency region represents the charge transfer resistance. The curvature radius of $MnMoO_4$-S in the high-frequency region is smaller than another, indicating the charge transfer resistance is smaller. In the low-frequency region, it is a straight line with a slope of about 1, which represents Weber impedance, which is the transfer efficiency of electrolyte ions on the electrode surface and in the solution. The result suggests that the ion conduction efficiency of the solution in the $MnMoO_4$-S system is higher.

$MnMoO_4$-S//AC asymmetric supercapacitor testing

In order to improve the operating potential window and obtain a higher energy density of the supercapacitor, the synthetic material and activated carbon were assembled asymmetrically.[50] An $MnMoO_4$-S//AC asymmetric supercapacitor was assembled in a beaker using activated carbon with an effective mass of 5.5 mg as the negative electrode and Ni foam with 1.0 mg $MnMoO_4$-S as the positive electrode.

Fig. 8a is the cyclic voltammetry curve of activated carbon and synthetic $MnMoO_4$-S. It shows that the specific capacitance of synthetic materials is much higher than that of activated carbon. Fig. 8b is the CV curve of the assembled asymmetric supercapacitor at different potential windows. A slight oxygen evolution peak appears at 1.7 V, so the operating potential window for the charge and discharge test of the asymmetric supercapacitor is set to 0–1.65 V. Fig. 8c is the CV curve of the assembled asymmetric supercapacitor at different scanning speeds under the potential window of 0–1.7 V. It is found that the positions of oxidation peak and reduction peak did not change, which proves that the assembled supercapacitor had

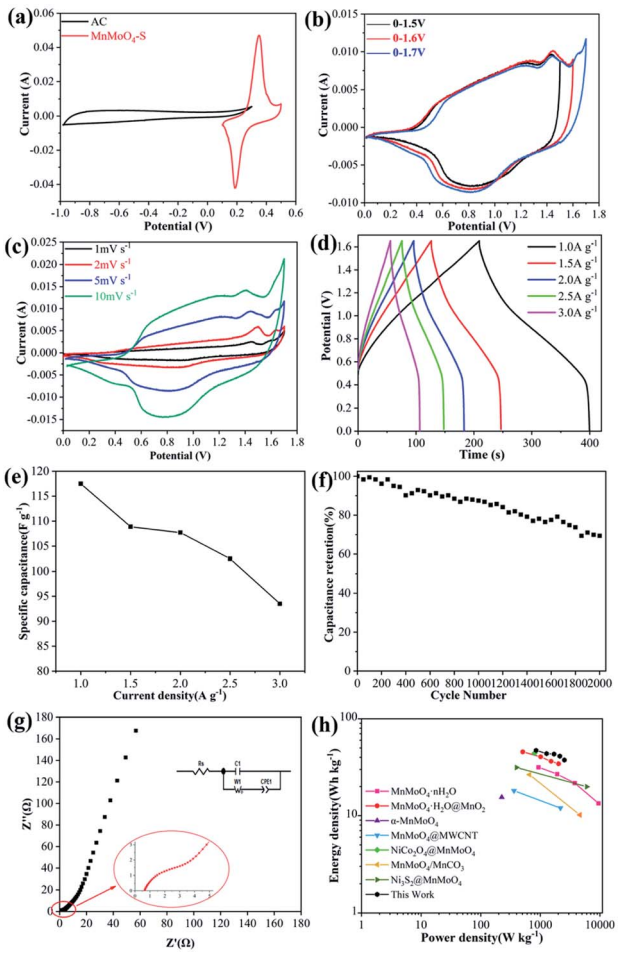

Fig. 8 (a) CV curves of AC and $MnMoO_4$-S; (b) CV curves of $MnMoO_4$-S//AC at different potential windows; (c) CV curves of the $MnMoO_4$-S//AC at various scan rates; (d) GCD curves of $MnMoO_4$-S//AC under different current densities; (e) specific capacitance at different current densities; (f) cycling stability; (g) Nyquist plot of $MnMoO_4$-S//AC and the inset shows corresponding electrical equivalent circuit; (h) Ragone plots of $MnMoO_4$-S//AC compared with other reported devices in the literature.

good stability. Fig. 8d shows the constant GCD curves of the supercapacitor. The basic shape of the charge–discharge curve does not change as the current density changes. The coulomb efficiency calculated by charging time over discharging time is always around 100%, which proves that the assembled capacitor has a good charge–discharge performance. According to the charge–discharge curves at 1 A g^{-1}, 1.5 A g^{-1}, 2 A g^{-1}, 2.5 A g^{-1} and 3 A g^{-1}, the capacitance of the assembled supercapacitor is calculated as 117.50 F g^{-1}, 108.88 F g^{-1}, 107.71 F g^{-1}, 102.51 F g^{-1}, and 93.51 F g^{-1}. At the current density of 3 A g^{-1}, the supercapacitor is charged and discharged 2000 times. With the increase in the number of cycles, the capacitance of the assembled capacitor decreases slowly. After 2000 cycles, the specific capacitance decreases to 69.36% of the initial capacitance value, mainly due to changes in electrolyte concentration over a long testing time. Fig. 8g is the Nyquist diagram of the supercapacitor, consisting of a semicircle section in the low frequency region and a straight section in the high frequency region. The cross-intercept, the radius of the semicircle, and the slope of the straight line represent the internal resistance, charge transfer resistance, and weber impedance, respectively. The circuit fitting with Zview software shows that the internal resistance $R_s = 0.19\ \Omega$ and the charge transfer resistance $R_{ct} = 1.36\ \Omega$. Fig. 8h is the Ragone diagram of the assembled capacitor, and the corresponding energy densities are 47.16, 43.70, 43.23, 41.25, and 37.53 W h kg^{-1} at the power densities of 849.98, 1274.92, 1700.06, 2125.05, and 2534.88 W kg^{-1}, respectively. According to the calculation using eqn (11) and (12),[51] compared with the asymmetric supercapacitors assembled by $MnMoO_4$ material and activated carbon in other literature, the supercapacitors have higher energy density at the same power density.[52–55]

$$E = \frac{1}{2}CV^2 \tag{11}$$

$$P = \frac{3600E}{\Delta t} \tag{12}$$

Conclusions

In this study, $MnMoO_4$-S nanosheets, which had rich oxygen vacancies due to a small amount of O being displaced by S, were grown *in situ* on nickel foam by a simple secondary hydrothermal method. Compared with the pure $MnMoO_4$ material, the addition of S causes more oxygen vacancies in the crystal, which increases the charge storage and electrical conductivity of the material. In addition, sulfur doping makes the valence state of the Mo element flexible, which is beneficial for increasing the pseudocapacitance so that the material has better electrochemical performance. In the three-electrode test, the specific capacitance of the $MnMoO_4$-S material reached 2526.7 F g^{-1} at 1 A g^{-1}, and the initial capacitance of the $MnMoO_4$-S material remained 95.56% after 2000 cycles of charge and discharge at 10 A g^{-1}. The composite material and the activated carbon electrode were used to simulate the assembly of asymmetric supercapacitors in a beaker. The specific capacitance of the assembled supercapacitor was 117.50 F g^{-1}, and the high energy density of 849.98 W kg^{-1} was obtained when the power density was 47.16 W h kg^{-1}. This means that MnMoO4-S material synthesized by a secondary hydrothermal method is a kind of electrode material with great application prospects for supercapacitors.

Conflicts of interest

There are no conflicts to declare.

Acknowledgements

This study was supported by the National Natural Science Foundation of China (granted 21376027).

References

1 X. Zhang, X. Sun, H. Zhang, D. Zhang and Y. Ma, *Mater. Chem. Phys.*, 2012, **137**, 290–296.
2 S. Faraji and F. N. Ani, *J. Power Sources*, 2014, **263**, 338–360.
3 Q. Zhu, D. Zhao, M. Cheng, J. Zhou and K. A. Owusu, *Adv. Energy Mater.*, 2019, **9**(36), 1901081.
4 Y. Xu, L. Ding, T. Zhong, X. Han, L. Jiao, H. Yuan and Y. Wang, *J. Energy Chem.*, 2015, **24**, 193–198.
5 S.-K. Chang, Z. Zainal, K.-B. Tan, N. A. Yusof, W. M. D. Wan Yusoff and S. R. S. Prabaharan, *Ceram. Int.*, 2015, **41**, 1–14.
6 P. B. Karandikar, D. B. Talange, U. P. Mhaskar and R. Bansal, *Energy*, 2012, **40**, 131–138.
7 A. Afif, S. M. H. Rahman, A. Tasfiah Azad, J. Zaini, M. A. Islan and A. K. Azad, *J. Energy Storage*, 2019, **25**, 100852.
8 C. Wu, Y. Zhu, M. Ding, C. Jia and K. Zhang, *Electrochim. Acta*, 2018, **291**, 249–255.
9 X. Ren, C. Guo, L. Xu, T. Li, L. Hou and Y. Wei, *ACS Appl. Mater. Interfaces*, 2015, **7**, 19930–19940.
10 Z. Xiao, L. Fan, B. Xu, S. Zhang, W. Kang, Z. Kang, H. Lin, X. Liu, S. Zhang and D. Sun, *ACS Appl. Mater. Interfaces*, 2017, **9**, 41827–41836.
11 O. Sadak, W. Wang, J. Guan, A. K. Sundramoorthy and S. Gunasekaran, *ACS Appl. Nano Mater.*, 2019, **2**, 4386–4394.
12 A. E. Elkholy, T. T. Duignan, X. Sun and X. S. Zhao, *ACS Appl. Energy Mater.*, 2021, **4**, 3210–3220.
13 L. Wang, G. Duan, J. Zhu, S. M. Chen, X. H. Liu and S. Palanisamy, *J. Colloid Interface Sci.*, 2016, **483**, 73–83.
14 J. Jiang, Y. Zhang, P. Nie, G. Xu, M. Shi, J. Wang, Y. Wu, R. Fu, H. Dou and X. Zhang, *Adv. Sustainable Syst.*, 2018, **2**, 1700110.
15 F. Liao, X. Han, Y. Zhang, C. Xu and H. Chen, *Ceram. Int.*, 2018, **44**, 22622–22631.
16 M. Isacfranklin, B. J. Rani, G. Ravi, R. Yuvakkumar, S. I. Hong, D. Velauthapillai and B. Saravanakumar, *ChemistrySelect*, 2020, **5**, 7728–7733.
17 I. Ayman, A. Rasheed, S. Ajmal, A. Rehman, A. Ali, I. Shakir and M. F. Warsi, *Energy Fuels*, 2020, **34**, 7622–7630.
18 V. Kalyani, S. Mondal, J. Saha and C. Subramaniam, *Nanoscale*, 2018, **10**, 3663–3672.
19 W. H. Low, P. S. Khiew, S. S. Lim, C. W. Siong and E. R. Ezeigwe, *J. Alloys Compd.*, 2019, **775**, 1324–1356.
20 T. Watcharatharapong, M. Minakshi Sundaram, S. Chakraborty, D. Li, G. M. Shafiullah, R. D. Aughterson and R. Ahuja, *ACS Appl. Mater. Interfaces*, 2017, **9**, 17977–17991.
21 X. Mu, Y. Zhang, H. Wang, B. Huang, P. Sun, T. Chen, J. Zhou, E. Xie and Z. Zhang, *Electrochim. Acta*, 2016, **211**, 217–224.
22 H. Cao, N. Wu, Y. Liu, S. Wang, W. Du and J. Liu, *Electrochim. Acta*, 2017, **225**, 605–613.
23 J. Tang, Y. Ge, J. Shen and M. Ye, *Chem. Commun.*, 2016, **52**, 1509–1512.
24 M. Yu, X. Li, Y. Ma, R. Liu, J. Liu and S. Li, *Appl. Surf. Sci.*, 2017, **396**, 1816–1824.
25 Z. Xie, L. Liu, Y. Li, D. Yu, L. Wei, L. Han, Y. Hua, C. Wang, X. Zhao and X. Liu, *J. Alloys Compd.*, 2021, **874**, 159860.
26 S. Alipour and M. Arvand, *Colloids Surf., A*, 2020, **606**, 125456.
27 F. Xiang, X. Zhou, X. Yue, Q. Hu, Q. Zheng and D. Lin, *Electrochim. Acta*, 2021, **379**, 138178.
28 Z. Xu, S. Sun, Y. Han, Z. Wei, Y. Cheng, S. Yin and W. Cui, *ACS Appl. Energy Mater.*, 2020, **3**, 5393–5404.
29 J. Yesuraj, V. Elumalai, M. Bhagavathiachari, A. S. Samuel, E. Elaiyappillai and P. M. Johnson, *J. Electroanal. Chem.*, 2017, **797**, 78–88.
30 K. K. Purushothaman, M. Cuba and G. Muralidharan, *Mater. Res. Bull.*, 2012, **47**, 3348–3351.
31 K. Xu, S. Ma, Y. Shen, Q. Ren, J. Yang, X. Chen and J. Hu, *Chem. Eng. J.*, 2019, **369**, 363–369.
32 T. Xing, Y. Ouyang, Y. Chen, L. Zheng, C. Wu and X. Wang, *J. Energy Storage*, 2020, **28**, 101248.
33 J. Xu, Y. Sun, M. Lu, L. Wang, J. Zhang, J. Qian and X. Liu, *Chem. Eng. J.*, 2018, **334**, 1466–1476.
34 H. Li, H. Xuan, Y. Guan, G. Zhang, R. Wang, X. Liang, Z. Xie, P. Han and Y. Wu, *Electrochim. Acta*, 2020, **345**, 136260.
35 S. Chen, G. Yang, Y. Jia and H. Zheng, *J. Mater. Chem. A*, 2017, **5**, 1028–1034.
36 X. Huang, W. Zhang, C. Zhou, L. Yang, H. Wang, Q. Gao and M. Zhu, *J. Colloid Interface Sci.*, 2020, **576**, 176–185.
37 Y. Cao, W. Li, K. Xu, Y. Zhang, T. Ji, R. Zou, J. Yang, Z. Qin and J. Hu, *J. Mater. Chem. A*, 2014, **2**, 20723–20728.
38 L. Gao, G. Chen, L. Zhang, B. Yan and X. Yang, *Electrochim. Acta*, 2021, **379**, 138185.
39 F. Nti, D. A. Anang and J. I. Han, *Mater. Lett.*, 2018, **217**, 146–150.
40 H. Wei, J. Yang, Y. Zhang, Y. Qian and H. Geng, *J. Colloid Interface Sci.*, 2018, **524**, 256–262.
41 Y. Wei, V. T. Tran, C. Zhao, H. Liu, J. Kong and H. Du, *ACS Appl. Mater. Interfaces*, 2019, **11**, 21445–21453.
42 J. Li, X. Xu, B. Huang, Z. Lou and B. Li, *ACS Appl. Mater. Interfaces*, 2021, **13**, 10047–10053.
43 S. Duraisamy, A. Ganguly, P. K. Sharma, J. Benson, J. Davis and P. Papakonstantinou, *ACS Appl. Nano Mater.*, 2021, **4**, 2642–2656.
44 S. Singh, J. Deb, U. Sarkar and S. Sharma, *ACS Sustainable Chem. Eng.*, 2021, **9**, 7328–7340.
45 Y. Chen, W. Yang, S. Gao, C. Sun and Q. Li, *ACS Appl. Nano Mater.*, 2018, **1**, 3565–3578.
46 X. Wang, H. Liu, M. Li, J. Li, Y. Lu, L. Wang, Z. Wang, X. Zhang and X. Ding, *Electrochim. Acta*, 2021, **390**, 138872.
47 F. Wang, D. Liu, J. Wen and X. Zheng, *J. Environ. Chem. Eng.*, 2021, **9**(5), 106042.
48 D. Cai, B. Liu, D. Wang, Y. Liu, L. Wang, H. Li, Y. Wang, C. Wang, Q. Li and T. Wang, *Electrochim. Acta*, 2014, **125**, 294–301.
49 D. Ghosh, S. Giri and C. K. Das, *Nanoscale*, 2013, **5**, 10428–10437.
50 R. Xu, J. Lin, J. Wu, M. Huang, L. Fan, X. He, Y. Wang and Z. Xu, *Electrochim. Acta*, 2017, **252**, 470–481.
51 S. Chen, S. Cui, S. Chandrasekaran, C. Ke, Z. Li, P. Chen, C. Zhang and Y. Jiang, *Electrochim. Acta*, 2020, **341**, 135893.

52 X. Lu, W. Jia, H. Chai, J. Hu, S. Wang and Y. Cao, *J. Colloid Interface Sci.*, 2019, **534**, 322–331.
53 J. Bhagwan, S. K. Hussain, B. N. V. Krishna and J. S. Yu, *J. Alloys Compd.*, 2021, **856**, 157874.
54 Y. Chen, Y. Li, Z. Hai, Y. Li, S. Kan, J. Chen, X. Chen, S. Zhuiykov, D. Cui and C. Xue, *Appl. Surf. Sci.*, 2018, **452**, 413–422.
55 M. R. Pallavolu, A. N. Banerjee, R. R. Nallapureddy and S. W. Joo, *J. Mater. Sci. Technol.*, 2022, **96**, 332–344.